

Solar-Driven Water Splitting at 13.8% Solar-to-Hydrogen Efficiency by an Earth-Abundant Electrolyzer

Joakim Ekspong, Christian Larsen, Jonas Stenberg, Wai Ling Kwong, Jia Wang, Jinbao Zhang, Erik M. J. Johansson, Johannes Messinger, Ludvig Edman, and Thomas Wågberg*



Cite This: *ACS Sustainable Chem. Eng.* 2021, 9, 14070–14078



Read Online

ACCESS |



Metrics & More



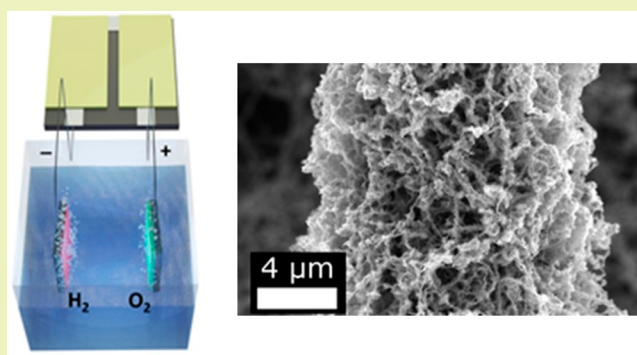
Article Recommendations



Supporting Information

ABSTRACT: We present the synthesis and characterization of an efficient and low cost solar-driven electrolyzer consisting of Earth-abundant materials. The trimetallic NiFeMo electrocatalyst takes the shape of nanometer-sized flakes anchored to a fully carbon-based current collector comprising a nitrogen-doped carbon nanotube network, which in turn is grown on a carbon fiber paper support. This catalyst electrode contains solely Earth-abundant materials, and the carbon fiber support renders it effective despite a low metal content. Notably, a bifunctional catalyst–electrode pair exhibits a low total overpotential of 450 mV to drive a full water-splitting reaction at a current density of 10 mA cm⁻² and a measured hydrogen Faradaic efficiency of ~100%. We combine the catalyst–electrode pair with solution-processed perovskite solar cells to form a lightweight solar-driven water-splitting device with a high peak solar-to-fuel conversion efficiency of 13.8%.

KEYWORDS: Solar-driven electrolysis, Earth-abundant materials, Nanostructured catalyst, Perovskite solar cells, Cost analysis



INTRODUCTION

The ever-increasing energy demand, spurred by an overall global increase in living standards and a larger world population estimated to reach 10 billion people in 2060, in combination with global warming, mandates a fast transition to renewable energy sources.¹ The Sun offers a continuous, albeit intermittent, source of energy, but the direct conversion of solar energy to electricity will not alone solve the energy demand, due to poorly developed electrical grids in large parts of the world and due to the fact that less than 20% of the energy consumption today is in the form of direct electricity.² Converting solar energy to transportable hydrogen fuel by solar-driven water electrolysis or photocatalysis are promising routes to lower fossil-fuel dependence, since the stored hydrogen can be used in fuel cells that convert the chemically stored energy back to electricity, with water as the only byproduct.^{3–8} Since H₂ has a very high gravimetric energy density, fuel cells are preferable for long distances and heavy transportation over battery-driven vehicles, and several countries are now rapidly developing an infrastructure for fueling vehicles by hydrogen.⁹ Besides usage as a high density energy carrier, H₂ can also be used in many industrial applications, such as producing CO₂-free steel and NH₃. However, around 95% of all hydrogen is today produced by reforming natural gas and coal gasification, releasing almost 1 Gt CO₂ to the atmosphere every year, with the consequence

being that the current hydrogen economy is far from CO₂ neutral.^{5,10} Solar-driven water electrolysis thus represents a potentially efficient way for CO₂-free hydrogen production.

Sustainable water electrolysis requires that the anode and cathode catalysts are noble metal free and contain small amounts of other metals in order to lower system costs and facilitate recycling. Using bifunctional catalysts that work for both hydrogen evolution and oxygen evolution is also advantageous since it facilitates upscaling. In alkaline conditions, transition metal oxides, based on Ni, Fe, and Co, have been shown to exhibit low overpotential for the oxygen evolution reaction (OER), in line with the best noble metal oxides RuO₂ and IrO₂, but few examples of such catalysts are reported for the hydrogen evolution reaction (HER),¹¹ although approaches such as vacancy engineering,^{12–15} bimetallic alloying, and addition of phosphides^{12,16} have shown to be promising strategies to lower the overpotential for metals toward HER in alkaline conditions.^{17,18} In recent years, the best catalyst electrodes are usually supported on

Received: June 2, 2021

Revised: September 23, 2021

Published: October 13, 2021



rather expensive nickel foams for achieving a high surface-area 3D network that concurrently is stable and relatively active as a catalyst itself.¹⁹ An alternative support is nanostructured, high surface-area carbon, as carbon is abundant, has a high conductivity, and a good ability to anchor nanocatalysts, especially if properly functionalized.^{20–22} However, at harsh alkaline conditions, the carbon at the anode is at risk of being oxidized, albeit this risk is lowered for crystalline carbon phases such as graphite or carbon nanotubes.^{23,24} Catalysts such as FeNi-layered double hydroxides feature low overpotential for OER and offer better stability than nanoparticles, since a layered structure could assist in protecting the carbon support against direct exposure to the alkaline electrolyte.^{25–27} Fe–Ni alloys, however, exhibit rather high overpotential for HER.

In this study, we investigate the effects of adding a third transition metal, molybdenum, to the Fe–Ni alloy. Previously, bimetallic transition metal alloys doped with a third high melting-point transition metal have shown good performance for OER, and molybdenum-based materials have in addition shown excellent performance as HER catalysts.^{11,17,28–33} Therefore, for further optimizing the performance of NiFe toward OER but also promote HER, molybdenum was added in the NiFe complex. Here, we report on the design of a trimetallic hybrid catalyst, which drives the water-splitting reaction at 10 mA cm⁻² at an overpotential as low as 450 mV. The low overall overpotential allows us to operate our complete water-splitting device, comprising our hybrid catalyst electrodes and two serially connected solution-processed perovskite solar cells, with a high solar-to-hydrogen conversion efficiency (STH) of 13.8%.

RESULTS AND DISCUSSION

To achieve our goal of an abundant electrode, we opted to use carbon paper (CP) comprising carbon fibers (with a typical diameter of 10–20 μm) as the starting material. The CP fibers allow for good anchor points for an extremely fine network of nitrogen-doped carbon nanotubes (NCNTs, typical diameter of 20–120 nm). The NCNTs were grown directly on the carbon fibers using chemical vapor deposition for achieving high adhesion and reduced contact resistance. An essential aspect for a well-coated catalyst structure is the high number of adhesion sites on the nitrogen-functionalized carbon nanotubes, which previously has been proven to be beneficial for catalysts anchoring.^{20–22} Furthermore, it has been shown that the introduced nitrogen defects in the NCNTs result in an increased electrical conductivity compared to pristine CNTs.³⁴ This combined support material, consisting of a carbon-based NCNT/CP network, provides a relatively large surface area (70 m²/g) with good conductivity, stability, and high density of anchoring sites for the metal catalysts.²¹

To finalize the catalyst electrode synthesis, a trimetallic NiFeMo catalyst was decorated onto the NCNT/CP support through hydrothermal synthesis (see [Experimental Section](#) for details). While NiFe hydroxides have been used as very efficient catalysts for OER previously, Mo oxides have shown near optimal hydrogen adsorption energies and are seen as promising candidates for HER in alkaline electrolytes and also as an OER catalyst.^{29,31,32} Therefore, we have added Mo as a third metal in the catalysts to improve the HER activity and still retain or improve the high OER activity of NiFe. The XPS data in [Figure S1](#) show that the Ni:Fe:Mo ratio is 1.1:1.0:0.4 with an oxygen:metal ratio of 2.05:1.00 in agreement with a metal oxide/hydroxide phase for the catalyst. The low-

magnification SEM image of the finished catalyst electrode in [Figure 1a](#) demonstrates a high yield of nanostructured catalysts and uniformly coated NCNTs throughout the CP substrate. The close-up in [Figure 1b](#) shows a single carbon fiber, with a diameter of 15–20 μm, densely covered by thin NCNTs, which are subsequently decorated by a homogeneous layered structure of the NiFeMo catalyst.

In [Figure 1c](#), the high-magnification SEM image of one single NiFeMo-coated NCNT reveals that it exhibits a nanoflake (NF) morphology of NiFeMo metals that are fully covering the NCNT. This conclusion is supported by the energy-dispersive X-ray spectroscopy (EDS) images shown in [Figure S2](#). We also note that the flake-like structure that is densely covering the nanotubes could protect the underlying carbon atoms from being oxidized at the anode during harsh operational conditions.³⁵ We refer to the NiFeMo/NCNT/CP catalyst electrode configuration as NiFeMo-NF. In order to investigate the role of Mo doping of the NiFe catalysts, we also synthesized a NiFe reference catalyst without any Mo on the NCNT/CP support but which otherwise followed the same synthesis procedure. This synthesis resulted mostly in particle-like NiFe structures covering the nanotubes (see SEM images in [Figure S3](#)), meaning that the Mo precursor also is important for achieving a layered nanoflake structure.

In order to prepare a HER electrode of seemingly similar metallic composition, the NiFeMo-NF electrode was reduced in Ar:H₂ (95:5) flow at 450 °C for 2 h and thereafter cooled in the same atmosphere before being retrieved. The reduction treatment resulted in a lowering of the total oxygen:metal ratio from 2.05:1.00 to 1.24:1.00 while also promoting reduced oxidation numbers in the metals along with pure metallic states (XPS, [Figure S1](#)). Similar reduction methods are commonly employed to activate HER catalysts such as in stainless steel, NiO, and NiMo catalysts, where the reduced material is found more active, as a result of more optimal adsorption energies

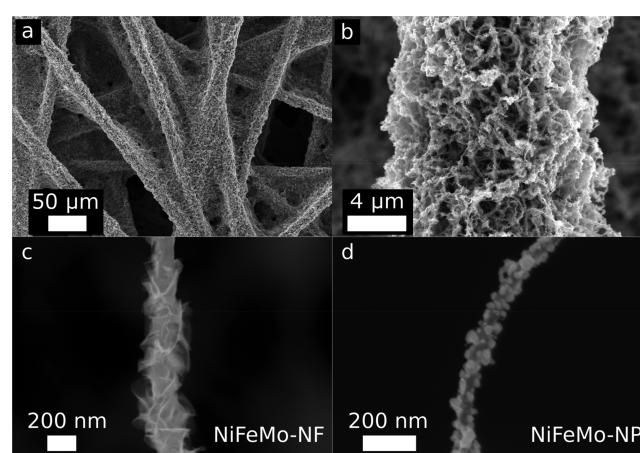


Figure 1. SEM images of the (a–c) NiFeMo-NF and (d) NiFeMo-NP catalysts. The (a) low magnification image reveals the overall catalyst electrode structure with CP fibers coated with NCNTs which in turn are decorated with the trimetallic NiFeMo catalyst. The close-up on a single CP fiber in (b) reveals the dense coating of NCNTs and a NiFeMo catalyst on the CP. The high magnification image in (c) of a single decorated NCNT on a NiFeMo-NF OER electrode reveals that the NCNT is densely covered with a nanoflake-structured NiFeMo catalyst. (d) The NiFeMo catalyst on the HER electrode has been subjected to a reduction process leading to a structural change from nanoflakes to nanoparticles, NiFeMo-NP.

and higher electrical conductivity.^{17,36,37} The nanoflake structures of the NiFeMo-NF catalysts are concurrently transformed into nanoparticle (NP) structures, as highlighted by the SEM images in Figure 1d. The SEM images also reveal that the catalyst particles remain firmly attached to the NCNT network with a homogeneous coverage of the NCNT/CP support, as indicated by the SEM-EDS images in Figure S2. The reduced catalyst electrode is denoted NiFeMo-NP.

To evaluate the electrochemical performance of each catalyst separately, 0.2 cm² pieces of the electrodes were punched out and connected in three-electrode cell setups with Ag/AgCl and Pt wire as the reference and the counter electrode, respectively. The measurements were performed in 1.0 M KOH with a 2 mV s⁻¹ scan speed. The performances of the individual NiFeMo-NP electrode in the HER and that of the NiFeMo-NF electrode in the OER are shown in Figure 2a and b, respectively. For comparison, the Mo-free NiFe catalysts anchored on a similar NCNT/CP support, blank NCNT/CP support as well as Pt wire (HER), and IrO₂ on CP (OER) were also measured. We note that for the NCNTs/CP support, there is no background currents at the gas production potentials, which indicates that the electrode is stable and inert at these conditions. Also, here the NiFe catalyst was reduced before HER tests.

Alloying NiFe with Mo leads to a significant increase in HER activity as manifested by a lowering of the overpotential needed to reach 10 mA cm⁻² from 250 mV for NiFe/NCNT/CP to 170 mV for NiFeMo-NP. The overpotentials for the noble metal-free hybrid catalyst are in fact only 105 mV higher than that for Pt wire at the same current density. We also note in agreement with our earlier study that the “blank” NCNT/CP support electrodes possess very poor catalytic activity for HER.²¹ A Tafel analysis of the voltammetry data (Figure S5a) indicates that the HER for both NiFeMo catalysts proceeds via a Volmer-Heyrovsky pathway, likely with strong hydrogen

adsorption manifested by a lack of a linear Tafel region at low current densities in the Tafel plot, and therefore, the Heyrovsky reaction step would be rate determining.^{38,39} A low Tafel slope of around 45 mV/dec is identified at low current densities for the Pt reference electrode. At higher current densities, the Tafel slope for all materials increases to 120 mV/dec, which is a general characteristic for metallic catalyst since the hydrogen coverage is then constant.³⁹

The OER activity of NiFeMo-NF shows a remarkable low potential at 10 mA cm⁻² of only 1.49 V (Figure 2b), which is superior to any of the tested reference materials including IrO₂ and comparable to the state-of-the-art catalysts.^{11,40} The small oxidation peak near 1.4 V likely corresponds to an oxidation reaction, similar to α -Ni(OH)₂ to γ -NiOOH transformation in pure nickel samples, although the exact origin is currently unclear due to the complexity of the trimetallic alloy.^{41–43} It is clear that the addition of NCNTs to the CP increases the electrode surface area, which in turn renders the normalized current density larger than for both Pt and IrO₂ on CP, manifesting the advantage of NCNT to boost the catalytic activity. The Tafel plot for NiFeMo-NF (Figure S5b) is harder to analyze since the oxidation peak is observed at relatively high current densities. Even though, if we extrapolate the current density, an initial Tafel slope of ~30 mV/dec at low current densities that increases to 60 mV/dec after the oxidation peak and then to 120 mV/dec can be observed, which is consistent with a metal–OOH to metal–OO⁻ reaction as the rate-determining step in the OER process.³⁸ However, the reaction mechanism for OER is normally difficult to confirm due to the high complexity. Similar behavior is seen for all tested materials, and the Tafel slopes eventually increase to greater than 300 mV/dec at larger current densities (~100 mA cm⁻²). In solar-driven electrolysis, these limitations are not necessarily of importance since the devices usually operate at the lower current densities produced by the solar cells, typically around 10 mA cm⁻².

To measure the performance for complete water splitting, the two catalysts were positioned parallel to each other at 1 cm separation. In this two-electrode setup (denoted NiFeMo-NF|NiFeMo-NP), the NiFeMo-NF was the anode and the NiFeMo-NP electrode the cathode. The scanning was done in the negative direction to eliminate any oxidation peaks that might overlap with the Faradaic current at low current densities. In Figure 2c, the polarization curve shows that for the full water-splitting reaction to occur only 1.68 V is required to reach 10 mA cm⁻², which represents a total overpotential of 450 mV for a current density of 10 mA cm⁻².

To certify that the measured current corresponds to gaseous production, the Faradaic efficiency (η_{H_2}) of the system was quantified by membrane-inlet mass spectrometry. A constant current density of 10 mA cm⁻² was applied to each of the catalysts, and the produced gases were measured at certain time intervals (detailed information in Experimental Section). The resulting efficiencies are shown in Figure 2d as solid green triangles (H₂) and solid green squares (O₂), while the corresponding black markers represent the quantified amount of produced gases. The Faradaic efficiencies were near 100% for both gases within experimental error. We find that the average molar ratio of hydrogen to oxygen produced in this experiment to be 2.06:1.00, which is close to the expected 2:1 ratio. Using the 100% Faradaic efficiency and the measured total overpotential of 450 mV at 10 mA cm⁻², we can conclude that the NiFeMo-NF|NiFeMo-NP electrode setup is able to

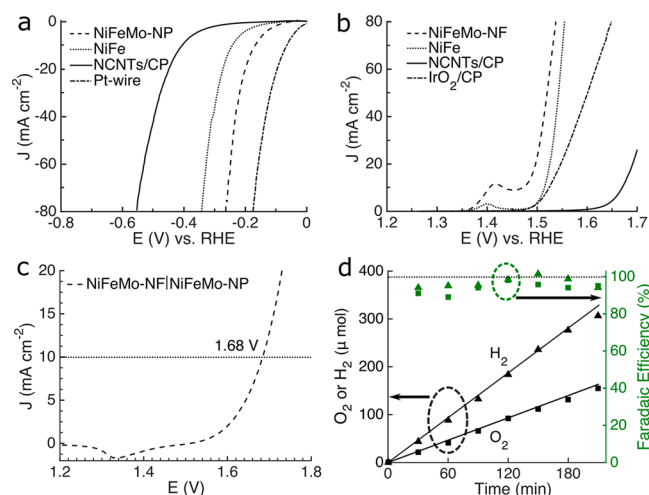


Figure 2. Electrochemical measurements showing the performance of the NiFeMo-NF and NiFeMo-NP catalyst electrodes for the (a) HER and the (b) OER. (c) Electrochemical measurement of the full water-splitting reaction catalyzed by NiFeMo-NF as the anode and NiFeMo-NP as the cathode. (d) Results from Faradaic efficiency measurements of each catalyst. The triangles correspond to H₂ and the squares to O₂. The solid lines show the theoretical amount of produced gases at 100% efficiencies. The electrolyte used in all experiments was 1.0 M KOH.

produce H_2 with an electric-to-hydrogen conversion efficiency of 73.2% at a production rate corresponding to a current density of 10 mA cm^{-2} .

The stability of the catalysts is important for applicability in real devices, and this was investigated by applying a steady current density of 10 mA cm^{-2} while monitoring the evolution of the applied potential of each catalyst electrode over a 10 h test period. We find that the catalyst electrodes are fairly stable as the combined overpotential for the NiFeMo-NF|NiFeMo-NP electrode pair increases from 1.68 to 1.78 V during the first 10 h of operation (Figure S5c), which arises from an overpotential increase of 40 mV for NiFeMo-NF and 60 mV for the NiFeMo-NP, corresponding to an overall performance decrease of 6%. From other studies on similar catalysts, such a decrease in performance, at relatively low current densities and potentials, is usually related to a lowering of the active catalyst surface area due to catalyst migration and catalyst dissolution.⁴⁴

We now turn our attention to the solar-driven hydrogen production device. To target the requirements of a low-cost, lightweight, and stand-alone system, we opted to use perovskite solar cells (PSCs) for the power generation. PSCs have recently emerged as potential low-cost competitors to traditional Si-based solar cells, thanks to their solution-based fabrication using only Earth-abundant materials for their active layers and their high solar-to-electric conversion efficiency.^{45–47} In addition, the high output voltage of PSCs renders for simpler (i.e., fewer devices connected in series) device configurations for water-splitting operations where a working potential of at least 1.23 V (not including the catalyst overpotentials) is required.^{48,49}

A schematic of the PSC device structure is presented in Figure 3a. The device consists of a mixed halide FAI:PbI₂:MABr:PbBr₂ (1:1.1:0.2:0.2 molar ratio) photoactive layer positioned in between a doped spiro-OMeTAD hole transport layer and a compact/mesoporous TiO₂ bilayer for the electron transport. The top Au cathode is in contact with the spiro-OMeTAD hole transport layer, whereas the bottom FTO anode is in contact with the TiO₂ bilayer. The FTO anode is deposited on a glass substrate, which provides mechanical stability. All layers were deposited by solution-based processes, with the exception of the vacuum-deposited Au cathode and FTO anode. The PSC fabrication protocol is detailed in the Experimental Section.

A total of 116 different PSC devices were fabricated and characterized under AM1.5 illumination, using a shadow mask

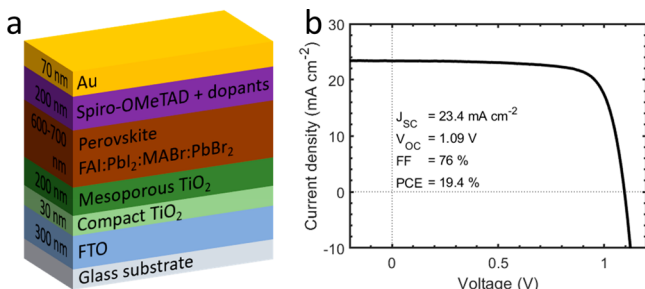


Figure 3. (a) Schematic of the perovskite solar cell structure. (b) J - V characteristics of the champion cell under AM1.5 illumination. The device features a large open-circuit voltage of 1.09 V and a high solar-to-electric power conversion efficiency of 19.4%. Additional performance metrics are presented in the inset.

with an opening of $A_{\text{PSC}} = 0.118 \text{ cm}^2$ to accurately define the illuminated area. Their performance is summarized in the histogram plots in Figure S6, and the narrow distributions of all of the performance metrics indicate a robust fabrication protocol. The current density–voltage (J - V) characteristic for our best performing PSC is shown in Figure 3b, and it features a short circuit current density of $J_{\text{SC}} = 23.4 \text{ mA cm}^{-2}$ (average $J_{\text{SC}} = 22.6 \text{ mA cm}^{-2}$), an open circuit voltage of $V_{\text{OC}} = 1.09 \text{ V}$ (average $V_{\text{OC}} = 1.05 \text{ V}$), and a solar-to-electric conversion efficiency of $\text{PCE} = 19.4\%$ (average $\text{PCE} = 17.5\%$). A high fill factor $\text{FF} = 76\%$ (average $\text{FF} = 73.5\%$) is the result of the sharp knee-like J - V trace, ensuring that a high operational voltage can be maintained when the illuminated solar cell is driving a load.

The J - V data for the PSC (Figure 3b) were matched with the J - V data of the two-terminal NiFeMo-NF|NiFeMo-NP catalyst pair (Figure 2c) in a load line analysis (Figure 4a) in order to predict the performance of a number of connected and complete solar-driven water-splitting devices. Specifically, the calculated solar-generated currents of two-, three-, and four-series-connected PSCs, with a constant total illuminated area of A_{PSC} , were compared with the calculated catalyst-consuming current of one NiFeMo-NF|NiFeMo-NP catalyst pair, with a varying active electrode area (A_{CAT}). The operation point for each configuration is found at the intersection between the PSC and the NiFeMo-NF|NiFeMo-NP catalyst-pair load lines. This analysis reveals that it is preferable to utilize a two-series connected PSC configuration for the complete solar-driven water-splitting device, because of the high V_{OC} and FF of the PSC in combination with the low overpotential of the NiFeMo-NF|NiFeMo-NP catalyst pair.

From the operating points derived by our load line analysis, we can extract the operating current (I_{OP}) which in turn (through the operating current density, $I_{\text{OP}}/A_{\text{PSC}}$) directly reveals the expected solar-to hydrogen conversion efficiency (STH) of our device via eq 1, as described in the Experimental Section. The calculated $I_{\text{OP}}/A_{\text{PSC}}$ (left y -axis) and the corresponding STH (right y -axis) are summarized in Figure 4c as a function of the $A_{\text{CAT}}/A_{\text{PSC}}$ ratio (i.e., an increase of catalyst area in comparison to the total PSC area). The data are plotted for the two-, three-, and four-series-connected PSCs. We again find that the two-series connected PSC results in the highest performance; specifically, that an $I_{\text{OP}}/A_{\text{PSC}} > 11 \text{ mA cm}^{-2}$, corresponding to an STH $> 13.5\%$, is obtained for $A_{\text{CAT}}/A_{\text{PSC}} > 1$. Increasing $A_{\text{CAT}}/A_{\text{PSC}}$ to much larger values than 1 result in a very small increase of STH, but with the drawback that the material cost of the catalyst increases. With these predictions at hand, we designed and fabricated a solar-driven water-splitting device comprising a two-series PSC, with a combined $A_{\text{PSC}} = 0.236 \text{ cm}^2$, and a NiFeMo-NF|NiFeMo-NP catalyst–electrode pair with $A_{\text{CAT}} = 2 \text{ cm}^2$, so that $A_{\text{CAT}}/A_{\text{PSC}} = 8.5$. This combination is marked with an open X in Figure 4c and predicts an $I_{\text{OP}}/A_{\text{PSC}} = 11.2 \text{ mA cm}^{-2}$, corresponding to an STH = 13.8%.

In order to experimentally test this prediction, two high-performance PSCs were electrically connected to the NiFeMo-NF|NiFeMo-NP catalyst–electrode pair, facing each other at a 4–5 mm interelectrode spacing. The catalyst electrodes were submerged into a 1 M KOH electrolyte, after which a constant AM1.5 illumination was directed at the PSCs. This activation of the two PSCs immediately switched on the generation of O_2 and H_2 gases at the catalyst electrodes by water splitting, as made visible by the bubble generation on the NiFeMo-NF

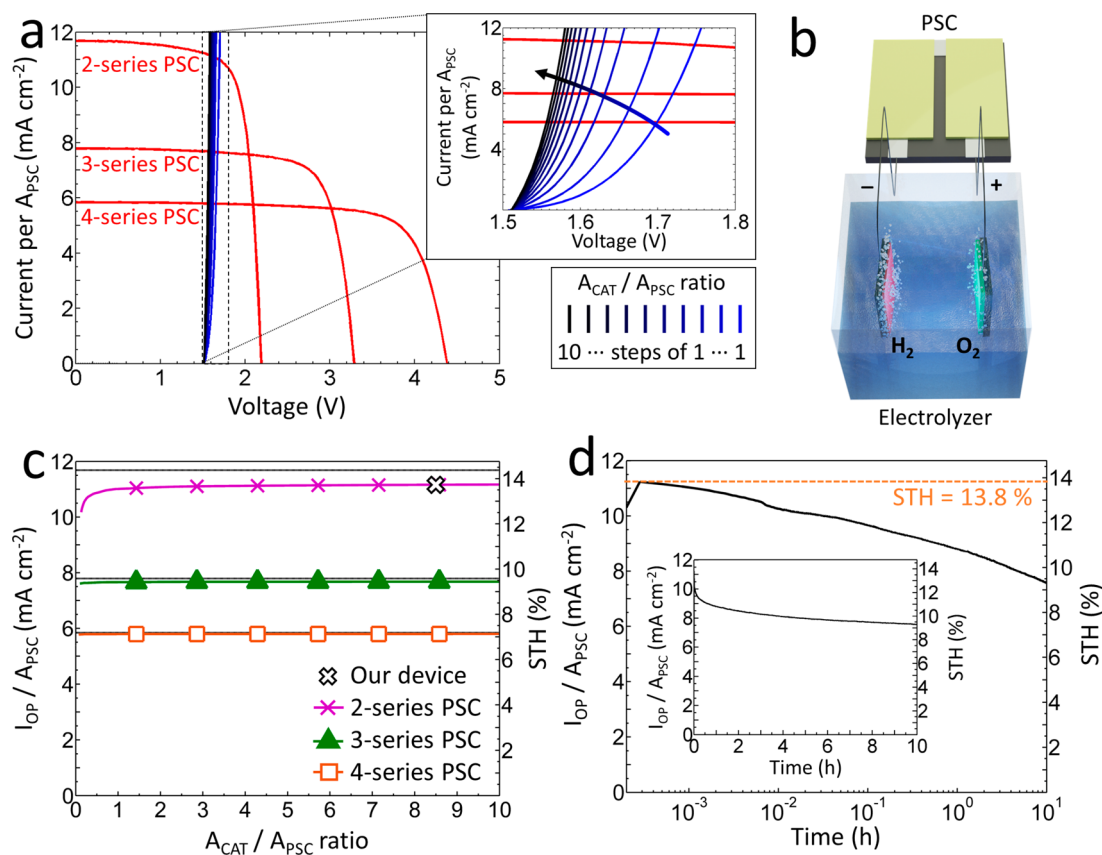


Figure 4. (a) Load line analysis of a solar-driven water-splitting device, as derived from measured J - V data of the PSC (Figure 3b) and the NiFeMo-NF|NiFeMo-NP catalyst-pair electrodes (Figure 2c), with the $A_{\text{CAT}}/A_{\text{PSC}}$ ratio increasing from 1 to 10, in steps of 1, as indicated by the arrow. The upper-right inset highlights the operation points, found at the intersections between the catalyst and PSC data, in the region between 1.5–1.8 V. (b) Schematic figure of the water-splitting device with the catalyst electrodes powered by two-series connected PSCs. (c) Calculated I_{OP} , normalized to the total PSC area (A_{PSC}), and STH for various configurations of the solar-driven water-splitting device. The configuration of our tested device, using a two-series connected PSC paired with NiFeMo-NF|NiFeMo-NP catalyst electrodes of $A_{\text{CAT}}/A_{\text{PSC}} = 8.5$, is indicated with an open X. (d) Measured $I_{\text{OP}}/A_{\text{PSC}}$ and STH during the 10 h long-term operation for our solar-driven water-splitting device under continuous AM1.5 illumination. The inset in (d) shows the same data on a linear time scale.

NiFeMo-NP catalyst electrodes (a photograph of the H₂-producing water-splitting device is shown in Figure S7). The measured initial value of $I_{\text{OP}}/A_{\text{PSC}}$ for the water-splitting device is 11.2 mA cm⁻², which corresponds to an STH of 13.8%. These measured numbers are in excellent agreement with the prediction from the load line analysis and demonstrate the validity of our analysis and, most importantly, the functionality of our developed solar-driven water-splitting device. The measured STH efficiency is improved compared to all previous electrolyzers driven by low-cost PSCs that used solely Earth-abundant electrocatalysts but lower compared to the highest performing perovskite/Si tandem devices that use noble metal electrocatalysts, which reached an initial efficiency of 17% STH.^{3,50–54} We note that in a longer perspective, using Earth-abundant electrocatalysts is necessary for sustainable large-scale H₂ production, both for cost-wise and environmental perspectives.⁵⁵

The stability of the water-splitting device is displayed in Figure 4d. A continuous decrease of $I_{\text{OP}}/A_{\text{PSC}}$ and STH during the 10 h measurement is observed, after a very short onset period originating from the shutter of the solar test system. Since the NiFeMo-NF|NiFeMo-NP catalyst electrodes alone demonstrate relatively stable operation during such time period (Figure S5c and d), we turn to the PSCs for an explanation. Figure S8 compares the $I_{\text{OP}}/A_{\text{PSC}}$ of the solar-

driven water-splitting device to the measured J_{SC} of a pristine two-series connected PSC during a continuous AM1.5 illumination stress test at short-circuit conditions. The data clearly reveal that the measured reduction in $I_{\text{OP}}/A_{\text{PSC}}$ matches the decline of J_{SC} , implying that the lowered water-splitting performance with time is primarily due to the degradation of the PSCs. We note that the PSCs were operated in ambient atmosphere without encapsulation and that various efforts into stabilizing nonencapsulated PSC devices are ongoing^{56–66} but are outside the scope of this study.

In addition to lab-scale demonstrations, there is also value in performing relevant cost analysis on the key components early on in development, simply to point out potential limitations and to motivate topics and set targets for future development. We therefore performed a rudimentary cost analysis focusing on the material costs for fabrication of the NiFeMo-NF|NiFeMo-NP catalyst-electrode pair and the PSC in two different scenarios: (i) a lab-scale scenario, with actual high-waste fabrication and actual lab-scale material costs and (ii) a no-waste scenario, with an estimated no-waste fabrication and actual material costs for similar quality materials. The cost analysis for the NiFeMo-NF|NiFeMo-NP catalyst-electrode pair and the PSC in these two scenarios is detailed in Table S2.

For the lab-scale fabrication scenario, we use actual material volumes and costs to calculate an enormous cost of \$19,100

m^{-2} of coated area for the catalyst–electrode pair. The more interesting cost-per-active-area metric for the catalyst (CPA_{CAT}) is obtained when the cost per coated m^2 is multiplied with the geometric fill factor (GFF), defined as the ratio between active and coated area. With a GFF = 89% for the lab-scale catalyst, we obtain a lab-scale $\text{CPA}_{\text{CAT}} = \$21,500 \text{ m}^{-2}$. Surprisingly, this high cost is mainly due to the high volume of DMF solvent used during the catalyst decoration step. For the PSC, we found an even more extreme cost of $\$43,400 \text{ m}^{-2}$. Considering the low GFF of 18.7%, this results in a cost-per-active-area for the PSC (CPA_{PSC}) of $\$233,000 \text{ m}^{-2}$. This cost is mainly driven by the high cost of the glass/FTO substrates and the material-inefficient deposition of the expensive spiro-OMeTAD and Au materials.

In the no-waste scenario, the material usage is calculated as the minimum amount of material needed to produce the lab-scale device structure by assuming 100% material utilization as well as reuse of solvents in the catalyst decoration step. This aims to investigate the effects of wasteful fabrication steps on the total cost. We find that no-waste fabrication of the catalyst–electrode pair results in a cost reduction of a factor of 35 to a cost of $\$540 \text{ m}^{-2}$ of coated area. The main cost driver is now the carbon paper as well as the catalyst precursors (mainly the Ni and Mo precursors). For the PSC, we find a cost reduction of a factor of 130 with a cost of $\$325 \text{ m}^{-2}$ of coated area. Here, the glass substrates, the spiro-OMeTAD, and Au are still the main culprits for the PSC.

On the basis of these results, we conclude that further development is needed in order to (i) significantly improve the stability of the PSCs and the catalysts, (ii) replace the expensive Au electrodes and glass substrates and develop low-cost alternatives to the spiro-OMeTAD for the PSCs, and (iii) develop solvent-efficient, low-waste, and large-scale fabrication of the PSC and catalysts. We finally note that such development is already ongoing.^{56,67–72}

CONCLUSIONS

We present the synthesis, characterization, and application of a solar-driven electrolyzer. The trimetallic NiFeMo catalyst takes the shape of nanometer-sized flakes anchored to a fully carbon-based current collector comprising a nitrogen-doped carbon nanotube network, which in turn is grown on a carbon fiber paper support. This catalyst electrode exhibits a low total overpotential for water splitting of 0.45 V at 10 mA cm^{-2} and combined with high-performance solution-processed PSCs forms a solar-driven water-splitting device with an impressive initial STH of 13.8%. We highlight that this performance is achieved with exclusively Earth-abundant materials making up the catalyst electrodes and a solar cell structure that is projected to allow for low-cost solution-based processing.

EXPERIMENTAL SECTION

Catalyst Synthesis. Thin films of Ti (10 nm) and Fe (5 nm) were thermally evaporated (Kurt J. Lesker PVD 75) on carbon paper (Sigracet GDL 34 AA). The carbon paper was then placed into a quartz tube (3 cm diameter) and inserted in a CVD chamber for NCNT growth. The thin metal films were reduced into small particles by heating the chamber to $800 \text{ }^\circ\text{C}$ in an Ar:H₂ (95:5) flow and then further reduced for 15 min with ammonia (25 mL min^{-1}). The NCNTs were grown at $800 \text{ }^\circ\text{C}$ with a 120 mL min^{-1} flow of Ar:H₂ (95:5) by injecting pyridine with a syringe (NEMSYS) at $10 \mu\text{L min}^{-1}$ for 45 min and then being cooled in Ar. To synthesize NiFeMo-NF, a small piece ($1.5 \text{ cm} \times 2 \text{ cm}$) of the coated carbon paper was mixed with a solution containing 6 mL of DMF and a total concentration of

3 mg mL^{-1} of Ni(acac)₂, Fe(acac)₃, and MoO₂(acac)₂ with a molar ratio of 5:1:0.4. The mixed solution together with the carbon paper was then inserted into a Teflon-lined autoclave and heated at $180 \text{ }^\circ\text{C}$ for 20 h before being cooled at room temperature and washed carefully with milli-Q water. To create NiFeMo-NP, the final material was further reduced by annealing in an Ar:H₂ (95:5) flow at $450 \text{ }^\circ\text{C}$ for 2 h and being cooled in the same reducing atmosphere before being taken out. The reference sample NiFe-NCNTs were synthesized following the same recipe without adding molybdenum.

Material Characterization. SEM was performed on a ZEISS Merlin FESEM microscope, and EDS was measured with an Oxford Instruments X-MAX 80 mm² X-ray detector at 5 kV. The XRD patterns were recorded with a Panalytical X'pert X-ray diffractometer with Cu K α radiation ($\lambda = 1.5418 \text{ \AA}$). XPS analyses were done on a Kratos axis ultradelay line detector electron spectrometer using a monochromatic Al K α source operated at 150 W.

Electrochemical Measurements. The polarization curves were recorded with linear sweep voltammetry at a scan rate of 2 mV s^{-1} in 1.0 M KOH with a potentiometer (Metrohm-Autolab PGSTAT302N, FRA32 M module). For analyzing individual electrodes, a three-electrode cell setup was used with Ag/AgCl (CHI111-CH instruments) as a reference electrode and a coiled Pt wire (99.999%) as the counter electrode. The voltage was converted into RHE by adding $0.222 \text{ V} + 0.059 \text{ pH}$ (pH 14). All polarization curves were postcorrected from the iR resistance ($2 \text{ } \Omega$) measured from electrochemical impedance spectroscopy. The scanning direction was positive for all polarization curves except for the full device setup, where any interfering oxidation is omitted by instead scanning in the negative direction.

Faradaic Efficiency. Membrane-inlet mass spectrometry (MIMS) was used to quantify the gas product of OER and HER, and its sensitivity toward O₂ and H₂ was calibrated using known amounts of air and a gas mixture of Ar:H₂ (95:5), respectively. The reference and counter electrodes were the Ag/AgCl/1 M KCl and Pt coil, respectively. A gastight electrochemical cell was used to house the WE and RE in the main compartment, which was separated by a glass frit from another compartment that housed the CE. Both compartments contained 1 M KOH as the electrolyte and were purged with N₂ for 1 h prior to measurement. Chronopotentiometry at -10 mA cm^{-2} (for HER) or 10 mA cm^{-2} (for OER) was performed for 4 h, during which the gaseous aliquots in the headspace of the main compartment were analyzed using MIMS at 30 min intervals. The sum of the gas in the headspace and electrolyte (calculated using Henry's law)⁷³ of the main compartment yielded the amount of gas product, which was compared with the value calculated from the assumption of perfect charge-to-O₂ (4-electron oxidation) or charge-to-H₂ (2-electron reduction) conversion to obtain the Faradaic efficiency.

Perovskite Solar Cell Fabrication. Fluorine-doped tin oxide (FTO)-coated glass substrates ($7 \text{ } \Omega \text{ sq}^{-1}$, Thin Film Devices, USA) were cleaned by 10 min subsequent steps of ultrasonication in detergent (Extran MA01):DI water (volume ratio 1:10), DI water, acetone, and isopropanol. A compact TiO₂ layer was deposited through spray pyrolysis by placing the clean and dry substrates on a hot plate (PZ28-3TD, Harry Gestigkeit) and raising the temperature stepwise to $500 \text{ }^\circ\text{C}$. A precursor solution comprising a mixture of 0.2 M titanium isopropoxide (>97.0%, Sigma-Aldrich) and 2 M acetylacetone (puriss >99.5%, Sigma-Aldrich) in isopropanol (IPA, anhydrous 99.5%, Sigma-Aldrich) with a volume ratio of 59.2:205.4:1000 was sprayed at a rate of $14 \mu\text{L s}^{-1}$ using a hand-held airbrush (Art. 17–372, Biltema), operated at $p = 20 \text{ psi}$, with a sweeping motion over the substrates at a 15 cm substrate-to-nozzle distance. After spray pyrolysis, the substrates were kept on the hot plate at $500 \text{ }^\circ\text{C}$ for 30 min for the TiO₂ to crystallize to the rutile phase (final thickness $\sim 30 \text{ nm}$) before slowly cooling to room temperature. A mesoporous TiO₂ was subsequently deposited by first spin-coating (spin speed = 4000 rpm, acceleration = 4000 rpm s^{-1} , time = 30 s) a 150 mg mL^{-1} precursor solution consisting of TiO₂ nanoparticles (DSL 18NR-T, Dyesol) dispersed in isopropanol

followed by annealing at 500 °C for 30 min (final thickness ~200 nm).

The perovskite solution consists of formamidinium iodide (FAI, Lumtec), methylammonium bromide (MABr, Lumtec), lead iodide (PbI₂, TCI chemicals), and lead bromide (PbBr₂, TCI chemicals) in a 1:1.1:0.2:0.2 M concentration of FAI:PbI₂:MABr:PbBr₂. The FAI:PbI₂ and MABr:PbBr₂ were dissolved separately in a mixture of *N,N*-dimethylformamid (DMF, anhydrous 99.8%, Sigma-Aldrich) and dimethyl sulfoxide (DMSO, anhydrous >99.9%, Sigma-Aldrich) with a volume ratio of 4:1, before they were stirred together at room temperature to form the perovskite solution. The perovskite solution was spin-coated in a N₂-filled glovebox ([O₂], [H₂O] < 1 ppm) using a two-step spin-coating process (step 1: spin speed = 1000 rpm, acceleration = 1000 rpm s⁻¹, time = 10 s. step 2: spin speed = 4000 rpm, acceleration = 1000 rpm s⁻¹, time = 30 s), and 65 μL of chlorobenzene (anhydrous 99.8%, Sigma-Aldrich) was quickly dropped onto the spinning substrate when there was 15 s left of step 2. The coated substrates were annealed at 100 °C for 1 h resulting in a uniform dark brown perovskite active layer film with a thickness of ~600–700 nm.

The hole transport layer comprised 2,2',7,7'-Tetrakis(*N,N*-di-*p*-methoxyphenylamino)-9,9'-spirobifluorene (spiro-OMeTAD, Lumtec) doped by bis(trifluoromethylsulfonyl)-imide lithium salt (Li-TFSI, Sigma-Aldrich), tris(2-(1H-pyrazol-1-yl)-4-*tert*-butylpyridine)-cobalt(III) tris(bis(trifluoromethylsulfonyl)-imide) (Co-TFSI, FK209, Dyenamo), and 4-*tert*-butylpyridine (TBP, Sigma-Aldrich). Li-TFSI and Co-TFSI were separately dissolved in acetonitrile (anhydrous 99.8%, Sigma-Aldrich) to a molar concentration of 2 and 0.5 M, respectively, before being added to form a 70 mM spiro-OMeTAD, 35 mM Li-TFSI, 2.1 mM Co-TFSI, and 231 mM TBP solution in chlorobenzene. The hole transport layer was deposited by spin-coating the solution (spin speed = 4000 rpm, acceleration = 1000 rpm s⁻¹, time = 30 s) on top of the perovskite layer resulting in a film thickness of ~200 nm. The substrates were then stored in a desiccator with a dry ambient atmosphere for 24 h before the device was finalized with a 70 nm gold electrode, deposited by thermal evaporation (*p* < 5 × 10⁻⁶ mbar). An FTO/Au electrode overlap of 3 mm × 7 mm defined the active device area.

Solar Simulator Measurements. The unencapsulated perovskite solar cells were illuminated using a solar simulator (Oriel sol 3A, Newport, model 940233 A) calibrated with a reference silicon solar cell (Newport, model 91150 V) to represent AM1.5 irradiance at *P*_{in} = 100 mW cm⁻². The electrical measurements were performed using a Labview controlled source measure unit (Keithley 2420). The illuminated area for each solar cell was restricted with a shadow mask to 0.118 cm² and the *I*–*V* characteristics were obtained using a forward-to-reverse bias sweep at a 20 mV s⁻¹ sweep rate. For the solar-driven water-splitting device, two perovskite solar cells (total illuminated active area *A*_{PSC} = 0.236 cm²) were connected in series and in turn connected to the NiFeMo-NF/NiFeMo-NP catalyst–electrode pair (*A*_{CAT} = 2 cm²). The catalyst electrodes were submerged in a 1 M KOH aqueous electrolyte at a 4–5 mm spacing. The operating current (*I*_{OP}) was measured in series with the catalyst and the solar cells during illumination, and a 100% Faradaic efficiency (*η*_{H₂}) was used when calculating the solar-to-hydrogen conversion efficiency (STH) through

$$\text{STH} = \frac{I_{\text{OP}}}{A_{\text{PSC}}} \cdot \frac{E_{0,\text{H}_2\text{O}} \eta_{\text{H}_2}}{P_{\text{in}}} \quad (1)$$

where *E*_{0,H₂O} = 1.23 V is the thermodynamic potential for water splitting.

■ ASSOCIATED CONTENT

SI Supporting Information

The Supporting Information is available free of charge at <https://pubs.acs.org/doi/10.1021/acssuschemeng.1c03565>.

XPS, SEM, XRD, electrochemical characterization, solar cell performance measurements, PV-driven electrolysis performance measurements, and cost analysis (PDF)

■ AUTHOR INFORMATION

Corresponding Author

Thomas Wågberg – Department of Physics, Umeå University, 901 87 Umeå, Sweden; orcid.org/0000-0002-5080-8273; Email: Thomas.wagberg@umu.se

Authors

Joakim Ekspong – Department of Physics, Umeå University, 901 87 Umeå, Sweden

Christian Larsen – Department of Physics, Umeå University, 901 87 Umeå, Sweden; orcid.org/0000-0002-2480-3786

Jonas Stenberg – Department of Physics, Umeå University, 901 87 Umeå, Sweden

Wai Ling Kwong – Department of Chemistry, Umeå University, 901 87 Umeå, Sweden; Department of Chemistry – Ångström Laboratory, Uppsala University, 751 20 Uppsala, Sweden; orcid.org/0000-0002-9732-8867

Jia Wang – Department of Physics, Umeå University, 901 87 Umeå, Sweden; orcid.org/0000-0001-8530-8132

Jinbao Zhang – Department of Chemistry – Ångström Laboratory, Uppsala University, 751 20 Uppsala, Sweden; College of Materials, Fujian Key Laboratory of Advanced Materials, Xiamen University, Xiamen, Fujian 361005, China

Erik M. J. Johansson – Department of Chemistry – Ångström Laboratory, Uppsala University, 751 20 Uppsala, Sweden; orcid.org/0000-0001-9358-8277

Johannes Messinger – Department of Chemistry, Umeå University, 901 87 Umeå, Sweden; Department of Chemistry – Ångström Laboratory, Uppsala University, 751 20 Uppsala, Sweden; orcid.org/0000-0003-2790-7721

Ludvig Edman – Department of Physics, Umeå University, 901 87 Umeå, Sweden; orcid.org/0000-0003-2495-7037

Complete contact information is available at:

<https://pubs.acs.org/doi/10.1021/acssuschemeng.1c03565>

Notes

The authors declare no competing financial interest.

■ ACKNOWLEDGMENTS

T.W. acknowledges support from Vetenskapsrådet (2017-04862) Energimyndigheten (45419-1), Artificial Leaf Project Umeå (Wallenberg). We thank the UCEM, VISIP, NanoLab, and XPS-KBC core facilities at Umeå University for support. L.E. acknowledges support from Vetenskapsrådet (2019-02345, 2017-04380), Energimyndigheten (50779-1) and Olle Engkvists stiftelse.

■ REFERENCES

- (1) World Population Prospects 2019, Rev. 1, 2019. *United Nations Department of Economic and Social Affairs*. https://population.un.org/wpp/Publications/Files/WPP2019_Highlights.pdf accessed October 2021).
- (2) World Energy Outlook 2019, 2019. *International Energy Agency*. <https://www.iea.org/reports/world-energy-outlook-2019> (accessed 2021-08-13).
- (3) Li, R. Latest progress in hydrogen production from solar water splitting via photocatalysis, photoelectrochemical, and photovoltaic

photoelectrochemical solutions. *Chinese Journal of Catalysis*. **2017**, *38*, 5–12.

(4) Chu, S.; Cui, Y.; Liu, N. The path towards sustainable energy. *Nat. Mater.* **2017**, *16*, 16–22.

(5) Dincer, I.; Acar, C. Review and evaluation of hydrogen production methods for better sustainability. *Int. J. Hydrogen Energy* **2015**, *40*, 11094–11111.

(6) Shaner, M. R.; Atwater, H. A.; Lewis, N. S.; McFarland, E. W. A comparative technoeconomic analysis of renewable hydrogen production using solar energy. *Energy Environ. Sci.* **2016**, *9*, 2354–2371.

(7) Jiang, C.; Moniz, S. J. A.; Wang, A.; Zhang, T.; Tang, J. Photoelectrochemical devices for solar water splitting - materials and challenges. *Chem. Soc. Rev.* **2017**, *46*, 4645–4660.

(8) Nikolaidis, P.; Poullikkas, A. A comparative overview of hydrogen production processes. *Renewable Sustainable Energy Rev.* **2017**, *67*, 597–611.

(9) Ball, M.; Weeda, M. The hydrogen economy – Vision or reality? *Int. J. Hydrogen Energy* **2015**, *40*, 7903–7919.

(10) Dutta, S. A review on production, storage of hydrogen and its utilization as an energy resource. *J. Ind. Eng. Chem.* **2014**, *20*, 1148–1156.

(11) McCrory, C. C.; et al. Benchmarking hydrogen evolving reaction and oxygen evolving reaction electrocatalysts for solar water splitting devices. *J. Am. Chem. Soc.* **2015**, *137*, 4347–4357.

(12) Kwong, W. L.; et al. Cationic Vacancy Defects in Iron Phosphide: A Promising Route toward Efficient and Stable Hydrogen Evolution by Electrochemical Water Splitting. *ChemSusChem* **2017**, *10*, 4544–4551.

(13) Zhang, C.; Shi, Y.; Yu, Y.; Du, Y.; Zhang, B. Engineering Sulfur Defects, Atomic Thickness, and Porous Structures into Cobalt Sulfide Nanosheets for Efficient Electrocatalytic Alkaline Hydrogen Evolution. *ACS Catal.* **2018**, *8*, 8077–8083.

(14) Zhang, T.; et al. Engineering oxygen vacancy on NiO nanorod arrays for alkaline hydrogen evolution. *Nano Energy* **2018**, *43*, 103–109.

(15) Zhao, Y.; et al. Defect-Engineered Ultrathin δ -MnO₂ Nanosheet Arrays as Bifunctional Electrodes for Efficient Overall Water Splitting. *Adv. Energy Mater.* **2017**, *7*, 1700005.

(16) Du, H.; Kong, R. M.; Guo, X.; Qu, F.; Li, J. Recent progress in transition metal phosphides with enhanced electrocatalysis for hydrogen evolution. *Nanoscale* **2018**, *10*, 21617–21624.

(17) McKone, J. R.; Sadtler, B. F.; Werlang, C. A.; Lewis, N. S.; Gray, H. B. Ni–Mo Nanopowders for Efficient Electrochemical Hydrogen Evolution. *ACS Catal.* **2013**, *3*, 166–169.

(18) Zeng, M.; Li, Y. Recent advances in heterogeneous electrocatalysts for the hydrogen evolution reaction. *J. Mater. Chem. A* **2015**, *3*, 14942–14962.

(19) Vij, V.; et al. Nickel-Based Electrocatalysts for Energy-Related Applications: Oxygen Reduction, Oxygen Evolution, and Hydrogen Evolution Reactions. *ACS Catal.* **2017**, *7*, 7196–7225.

(20) Sharifi, T.; et al. Hierarchical self-assembled structures based on nitrogen-doped carbon nanotubes as advanced negative electrodes for Li-ion batteries and 3D microbatteries. *J. Power Sources* **2015**, *279*, 581–592.

(21) Ekspong, J.; et al. Stabilizing Active Edge Sites in Semicrystalline Molybdenum Sulfide by Anchorage on Nitrogen-Doped Carbon Nanotubes for Hydrogen Evolution Reaction. *Adv. Funct. Mater.* **2016**, *26*, 6766–6776.

(22) Zamudio, A.; et al. Efficient Anchoring of Silver Nanoparticles on N-Doped Carbon Nanotubes. *Small* **2006**, *2*, 346–350.

(23) Wang, W.; Luo, J.; Chen, S. Carbon oxidation reactions could misguide the evaluation of carbon black-based oxygen-evolution electrocatalysts. *Chem. Commun. (Cambridge, U. K.)* **2017**, *53*, 11556–11559.

(24) Lu, X.; Yim, W. L.; Suryanto, B. H.; Zhao, C. Electrocatalytic oxygen evolution at surface-oxidized multiwall carbon nanotubes. *J. Am. Chem. Soc.* **2015**, *137*, 2901–2907.

(25) Gong, M.; et al. An advanced Ni-Fe layered double hydroxide electrocatalyst for water oxidation. *J. Am. Chem. Soc.* **2013**, *135*, 8452–8455.

(26) Song, F.; Hu, X. Exfoliation of layered double hydroxides for enhanced oxygen evolution catalysis. *Nat. Commun.* **2014**, *5*, 4477.

(27) Liu, L.; Wu, H.; She, L. Tuning Microstructures of Iron-Nickel Alloy Catalysts for Efficient Oxygen Evolution Reaction. *Chem. J. Chin. Univ.* **2020**, *41*, 1083–1090.

(28) Zhang, B.; et al. Homogeneously dispersed, multimetal oxygen-evolving catalysts. *Science* **2016**, *352*, 333–337.

(29) Jin, Y.; et al. Porous MoO₂ Nanosheets as Non-noble Bifunctional Electrocatalysts for Overall Water Splitting. *Adv. Mater.* **2016**, *28*, 3785–3790.

(30) Krstajić, N. V.; et al. Non-noble metal composite cathodes for hydrogen evolution. Part I: The Ni–MoO_x coatings electrodeposited from Watt's type bath containing MoO₃ powder particles. *Int. J. Hydrogen Energy* **2011**, *36*, 6441–6449.

(31) Luo, Z.; et al. Mesoporous MoO_{3-x} Material as an Efficient Electrocatalyst for Hydrogen Evolution Reactions. *Adv. Energy Mater.* **2016**, *6*, 1600528.

(32) Jin, Y.; Shen, P. K. Nanoflower-like metallic conductive MoO₂ as a high-performance non-precious metal electrocatalyst for the hydrogen evolution reaction. *J. Mater. Chem. A* **2015**, *3*, 20080–20085.

(33) Tian, J.; et al. Self-supported NiMo hollow nanorod array: an efficient 3D bifunctional catalytic electrode for overall water splitting. *J. Mater. Chem. A* **2015**, *3*, 20056–20059.

(34) Wiggins-Camacho, J. D.; Stevenson, K. J. Effect of Nitrogen Concentration on Capacitance, Density of States, Electronic Conductivity, and Morphology of N-Doped Carbon Nanotube Electrodes. *J. Phys. Chem. C* **2009**, *113*, 19082–19090.

(35) Fabbri, E.; Haberer, A.; Waltar, K.; Kötz, R.; Schmidt, T. J. Developments and perspectives of oxide-based catalysts for the oxygen evolution reaction. *Catal. Sci. Technol.* **2014**, *4*, 3800–3821.

(36) Ekspong, J.; Wagberg, T. Stainless Steel as a Bi-Functional Electrocatalyst-A Top-Down Approach. *Materials* **2019**, *12*, 2128.

(37) Gong, M.; et al. Nanoscale nickel oxide/nickel heterostructures for active hydrogen evolution electrocatalysis. *Nat. Commun.* **2014**, *5*, 4695.

(38) Shinagawa, T.; Garcia-Esparza, A. T.; Takanabe, K. Insight on Tafel slopes from a microkinetic analysis of aqueous electrocatalysis for energy conversion. *Sci. Rep.* **2015**, *5*, 13801.

(39) Ekspong, J.; Gracia-Espino, E.; Wågberg, T. Hydrogen Evolution Reaction Activity of Heterogeneous Materials: A Theoretical Model. *J. Phys. Chem. C* **2020**, *124*, 20911–20921.

(40) Suen, N.-T.; et al. Electrocatalysis for the oxygen evolution reaction: recent development and future perspectives. *Chem. Soc. Rev.* **2017**, *46*, 337–365.

(41) Hall, D. S.; Lockwood, D. J.; Bock, C.; MacDougall, B. R. Nickel hydroxides and related materials: a review of their structures, synthesis and properties. *Proc. R. Soc. London, Ser. A* **2015**, *471*, 20140792.

(42) Dionigi, F.; Strasser, P. NiFe-Based (Oxy)hydroxide Catalysts for Oxygen Evolution Reaction in Non-Acidic Electrolytes. *Adv. Energy Mater.* **2016**, *6*, 1600621.

(43) Trotochaud, L.; Young, S. L.; Ranney, J. K.; Boettcher, S. W. Nickel–Iron Oxyhydroxide Oxygen-Evolution Electrocatalysts: The Role of Intentional and Incidental Iron Incorporation. *J. Am. Chem. Soc.* **2014**, *136*, 6744–6753.

(44) Costa, J. D.; et al. Electrocatalytic Performance and Stability of Nanostructured Fe–Ni Pyrite-Type Diphosphide Catalyst Supported on Carbon Paper. *J. Phys. Chem. C* **2016**, *120*, 16537–16544.

(45) Kojima, A.; Teshima, K.; Shirai, Y.; Miyasaka, T. Organometal halide perovskites as visible-light sensitizers for photovoltaic cells. *J. Am. Chem. Soc.* **2009**, *131*, 6050–6051.

(46) Lee, M. M.; Teuscher, J.; Miyasaka, T.; Murakami, T. N.; Snaith, H. J. Efficient hybrid solar cells based on meso-superstructured organometal halide perovskites. *Science* **2012**, *338*, 643–647.

- (47) Burschka, J.; et al. Sequential deposition as a route to high-performance perovskite-sensitized solar cells. *Nature* **2013**, *499*, 316–319.
- (48) Nocera, D. G. The artificial leaf. *Acc. Chem. Res.* **2012**, *45*, 767–776.
- (49) Reece, S. Y.; et al. Wireless solar water splitting using silicon-based semiconductors and earth-abundant catalysts. *Science* **2011**, *334*, 645–648.
- (50) Sharifi, T.; et al. Toward a Low-Cost Artificial Leaf: Driving Carbon-Based and Bifunctional Catalyst Electrodes with Solution-Processed Perovskite Photovoltaics. *Adv. Energy Mater.* **2016**, *6*, 1600738.
- (51) Li, Z.; et al. Hybrid Perovskite-Organic Flexible Tandem Solar Cell Enabling Highly Efficient Electrocatalysis Overall Water Splitting. *Adv. Energy Mater.* **2020**, *10*, 2000361.
- (52) Karuturi, S. K.; et al. Over 17% Efficiency Stand-Alone Solar Water Splitting Enabled by Perovskite-Silicon Tandem Absorbers. *Adv. Energy Mater.* **2020**, *10*, 2000772.
- (53) Luo, J.; et al. Water photolysis at 12.3% efficiency via perovskite photovoltaics and Earth-abundant catalysts. *Science* **2014**, *345*, 1593–1596.
- (54) Luo, J.; et al. Bipolar Membrane-Assisted Solar Water Splitting in Optimal pH. *Adv. Energy Mater.* **2016**, *6*, 1600100.
- (55) Zou, X.; Zhang, Y. Noble metal-free hydrogen evolution catalysts for water splitting. *Chem. Soc. Rev.* **2015**, *44*, 5148–5180.
- (56) Boyd, C. C.; Cheacharoen, R.; Leijtens, T.; McGehee, M. D. Understanding Degradation Mechanisms and Improving Stability of Perovskite Photovoltaics. *Chem. Rev.* **2019**, *119*, 3418–3451.
- (57) Juarez-Perez, E. J.; et al. Photodecomposition and thermal decomposition in methylammonium halide lead perovskites and inferred design principles to increase photovoltaic device stability. *J. Mater. Chem. A* **2018**, *6*, 9604–9612.
- (58) Ciccioli, A.; Latini, A. Thermodynamics and the Intrinsic Stability of Lead Halide Perovskites CH₃NH₃PbX₃. *J. Phys. Chem. Lett.* **2018**, *9*, 3756–3765.
- (59) Samu, G. F.; Janáky, C.; Kamat, P. V. A Victim of Halide Ion Segregation. How Light Soaking Affects Solar Cell Performance of Mixed Halide Lead Perovskites. *ACS Energy Letters* **2017**, *2*, 1860–1861.
- (60) Latini, A.; Gigli, G.; Ciccioli, A. A study on the nature of the thermal decomposition of methylammonium lead iodide perovskite, CH₃NH₃PbI₃: an attempt to rationalise contradictory experimental results. *Sustainable Energy & Fuels* **2017**, *1*, 1351–1357.
- (61) Shao, Y.; et al. Grain boundary dominated ion migration in polycrystalline organic–inorganic halide perovskite films. *Energy Environ. Sci.* **2016**, *9*, 1752–1759.
- (62) Juarez-Perez, E. J.; Hawash, Z.; Raga, S. R.; Ono, L. K.; Qi, Y. Thermal degradation of CH₃NH₃PbI₃ perovskite into NH₃ and CH₃I gases observed by coupled thermogravimetry–mass spectrometry analysis. *Energy Environ. Sci.* **2016**, *9*, 3406–3410.
- (63) Brunetti, B.; Cavallo, C.; Ciccioli, A.; Gigli, G.; Latini, A. On the Thermal and Thermodynamic (In)Stability of Methylammonium Lead Halide Perovskites. *Sci. Rep.* **2016**, *6*, 31896.
- (64) Zhang, Y.; et al. Charge selective contacts, mobile ions and anomalous hysteresis in organic–inorganic perovskite solar cells. *Mater. Horiz.* **2015**, *2*, 315–322.
- (65) Han, Y.; et al. Degradation observations of encapsulated planar CH₃NH₃PbI₃ perovskite solar cells at high temperatures and humidity. *J. Mater. Chem. A* **2015**, *3*, 8139–8147.
- (66) Azpiroz, J. M.; Mosconi, E.; Bisquert, J.; De Angelis, F. Defect migration in methylammonium lead iodide and its role in perovskite solar cell operation. *Energy Environ. Sci.* **2015**, *8*, 2118–2127.
- (67) Svanstrom, S.; et al. Degradation Mechanism of Silver Metal Deposited on Lead Halide Perovskites. *ACS Appl. Mater. Interfaces* **2020**, *12*, 7212–7221.
- (68) Li, G.-R.; Gao, X.-P. Low-Cost Counter-Electrode Materials for Dye-Sensitized and Perovskite Solar Cells. *Adv. Mater.* **2020**, *32*, 1806478.
- (69) Zhang, Y.; Ng, S.-W.; Lu, X.; Zheng, Z. Solution-Processed Transparent Electrodes for Emerging Thin-Film Solar Cells. *Chem. Rev.* **2020**, *120*, 2049–2122.
- (70) Zhang, J.; et al. The Role of 3D Molecular Structural Control in New Hole Transport Materials Outperforming Spiro-OMeTAD in Perovskite Solar Cells. *Adv. Energy Mater.* **2016**, *6*, 1601062.
- (71) Tan, H.; et al. Efficient and stable solution-processed planar perovskite solar cells via contact passivation. *Science* **2017**, *355*, 722–726.
- (72) Schmidt, T. M.; Larsen-Olsen, T. T.; Carlé, J. E.; Angmo, D.; Krebs, F. C. Upscaling of Perovskite Solar Cells: Fully Ambient Roll Processing of Flexible Perovskite Solar Cells with Printed Back Electrodes. *Adv. Energy Mater.* **2015**, *5*, 1500569.
- (73) Sander, R. Compilation of Henry's law constants (version 4.0) for water as solvent. *Atmos. Chem. Phys.* **2015**, *15*, 4399–4981.